J. Fluid Mech. (2001), *vol.* 439, *pp.* 57–85. Printed in the United Kingdom

Gentle spilling breakers: crest flow-field evolution

By HAIBING QIAO AND JAMES H. DUNCAN

Department of Mechanical Engineering, University of Maryland, College Park, MD 20742, USA

(Received 16 April 1999 and in revised form 1 December 2000)

The flow fields at the crests of mechanically generated gentle spilling breakers are studied experimentally with particle image velocimetry (PIV). During the initial development of the breaker, a bulge forms on the forward face of the wave near the crest. The present measurements show that the flow field in this bulge is wavelike in nature and that the maximum horizontal component of the fluid velocity, u_{max}, is less than the wave crest speed. No vorticity is found during this stage of the breaking process. After a short while, the leading edge (called the toe) of the bulge begins to move rapidly down the wave crest; u_{max} reaches the speed of the wave crest just as the toe begins to move. Concurrent with the beginning of the toe motion, a vortical region appears at the free surface just downstream of the toe. At about the point in the wave development where the measurements end, the vortical region extends from the toe to the crest.

1. Introduction

The surface profile histories of gentle spilling breakers were studied experimentally by Duncan *et al.* (1994*a*, *b*, 1999). In these investigations, the waves were generated mechanically with a dispersive focusing method; three average wave packet frequencies ($f_0 = 1.15$, 1.26 and 1.42 Hz) and two or three wavemaker amplitudes at each frequency were used. It was found that as the wave steepens, the crest becomes asymmetric and a bulge appears at the crest on the forward face (see figure 1). During the growth of the bulge, its leading edge, called the toe, remains fairly stationary with respect to the crest while the amplitude of the bulge increases. Concurrent with the growth of the bulge, capillary waves appear and grow in amplitude upstream of the toe. After a short time, the toe begins a rapid motion down the wave face and the water surface between the toe and the crest quickly acquires a random appearance, indicating that the flow has become turbulent. It was found that the lengths of the capillary waves and the bulge are independent of f_0 and the wavemaker amplitude. Thus, the lengths of these features on the wave crests were found to scale with $\ell_c = \sqrt{T/g}$ where T is the surface tension divided by the fluid density and g is gravity. The experimental results are in qualitative agreement with the theoretical studies of Longuet-Higgins (see Longuet-Higgins 1992, 1996 and Longuet-Higgins & Cleaver 1994). A review of this literature can be found in the introduction to Duncan *et al.* (1999).

The present work is a continuation of the investigation of spilling breakers found in Duncan *et al.* (1999). The experimental facility, all the experimental techniques and nearly all the parameters used to generate the waves in the present study are identical to those in the previous work. However, in the present study, instead of investigating the surface profile history, the evolution of the flow field and vorticity field in the vicinity of the crest are explored. The flow fields are measured with particle image

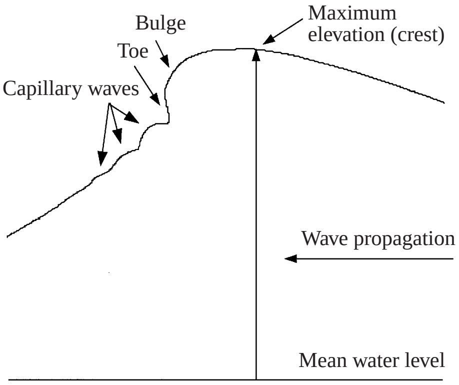

FIGURE 1. Schematic showing wave shape and nomenclature.

velocimetry (PIV). The flow fields in the crests of two-dimensional steady breakers have been measured by Lin & Rockwell (1995) and Dabiri & Gharib (1997) using PIV. The present measurements for unsteady spilling breakers bear some similarity to the steady case and in the following, similarities and differences are pointed out where appropriate.

The remainder of this paper is divided into four sections. In § 2, the PIV technique is described along with a listing of the experimental parameters used to generate the waves. In § 3, the flow field and vorticity field measurements for the 1.42 Hz wave are presented and discussed. These results are compared to those for the other two wave frequencies in § 4. Finally, the conclusions are presented in § 5.

2. Experimental details

2.1. *The wave tank and wave generation method*

The experiments were performed in a tank that is 14.8 m long, 1.22 m wide and 1.0 m deep (see figure 2). The waves were generated mechanically with a computer-controlled vertically oscillating wedge which spans the width of the tank at one end. The wedge motion was programmed to create wave packets that focused owing to dispersion effects thus creating breaking waves. The water surface was kept relatively free of ambient surfactants by continuous skimming and the surface tension was monitored with a Whilhelmy plate in combination with an *in situ* Langmuir trough. Detailed descriptions of the equipment and experimental techniques are given in Duncan *et al.* (1999).

2.2. *PIV equipment and procedures*

The flow fields at the crests of the waves were measured with PIV. The light source for the PIV photographs was a dual Nd:YAG laser system. The laser system consists of two separate lasers; each laser produces 200 mJ 10 ns pulses at a 30 Hz repetition rate. A time delay circuit was used to control the phase separation between the pulses of the two lasers. This time delay was adjusted and calibrated to within 1% of its set value by using an oscilloscope. In all cases reported herein, the time delay ranged between 0.4 ms and 0.5 ms (see table 1). The light beams from the two lasers were made co-linear by a series of optical components and the resulting beam was converted into a thin light sheet by a set of cylindrical lenses. The light sheet entered the wave tank through the bottom of the glass sidewall (see figure 2). An underwater

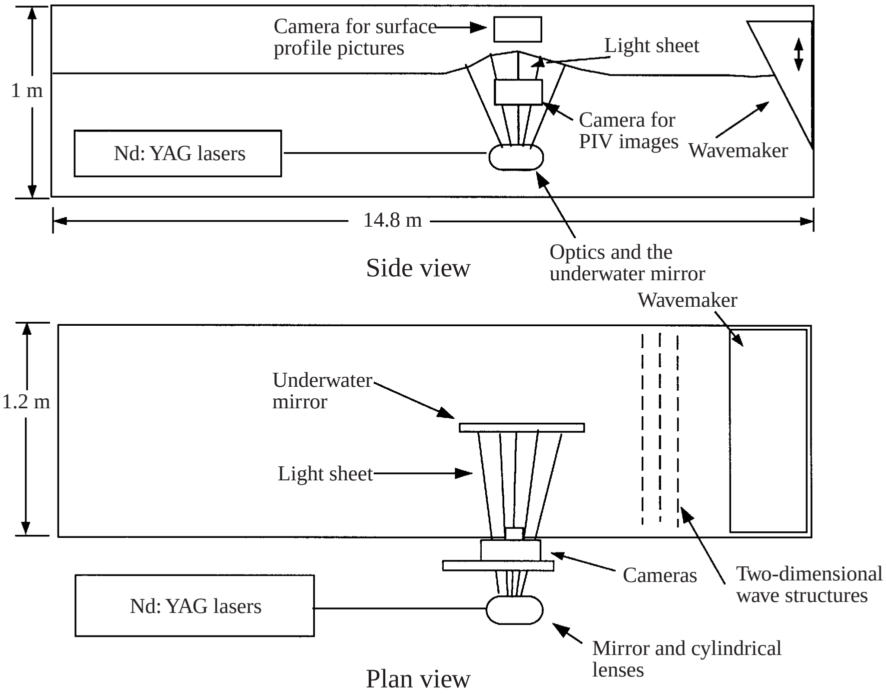

FIGURE 2. Schematic showing tank, wavemaker and optical set-up.

f_0 (Hz)	λ_0 (cm)	A/λ_0	Δt (ms)
1.42	77.43	0.0494	0.50
1.26	98.34	0.0495	0.45
1.15	118.06	0.0497 & 0.0502	0.40

TABLE 1. Experimental conditions. f_0 is the average frequency of the wavemaker motion, $\lambda_0 = g/(2\pi f_0^2)$, A is the overall amplitude of the wavemaker motion, and Δt is the time delay between laser pulses.

mirror was used to deflect the light sheet so that it was vertical, aligned with the direction of wave travel, and at a distance of about 35 cm from the glass wall. The thickness of the light sheet (δ) was about 1.5 mm in the measurement area. Fluid motion normal to the plane of the light sheet can result in single rather than double images of some particles, thus reducing the ability of the computational algorithm to find the velocity in a given PIV interrogation window. However, with the light sheet thickness $\delta = 1.5$ mm and the time delay between laser pulses $\Delta t = 0.5$ ms, it is expected that 90% of the particles located in the light sheet during the first laser pulse will still be within the light sheet thickness during the second laser pulse if the particle velocity component normal to the light sheet is less than $0.1\delta/\Delta t = 0.3\,\mathrm{m\,s^{-1}}$. This condition is expected to be amply satisfied in the present experiments, as is confirmed by analysis of the resulting PIV images.

The images of the particles were captured with a Nikon F3 35 mm camera with an f/2.8, 200 mm fixed-focal-length lens. Kodak T-Max ASA400 black and white film was used. The aperture of the camera was set at either f/16 or f/22. The camera

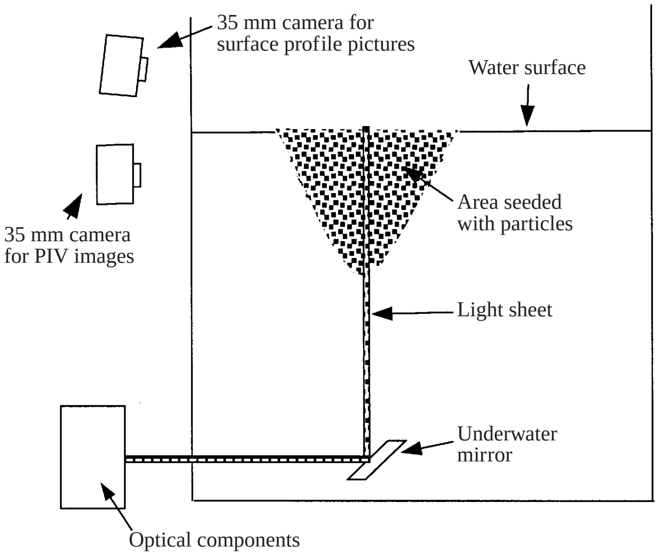

Figure 3. Schematic showing PIV measurement set-up.

pointed in the direction which is parallel to the wave crest line with a look up angle of about 1° (see figure 3). A second Nikon F3 35 mm camera was used to capture the surface profile of the wave crest at the same time as the PIV image was taken. This camera looked down from above the free surface with an angle of about 3° from the horizontal (see figure 3). The surface profile pictures taken by the second camera were used only to determine the toe position and breaking stage by comparing with the surface profiles in Duncan *et al.* (1999); they were not used to determine the position of the free surface in the PIV images taken by the first camera. Both cameras were stationary relative to the wave tank. The computer that controlled the wavemaker (see Duncan *et al.* 1999) also triggered an electronic circuit that controlled the timing of the cameras and laser light pulses. The correct timing values for the camera and lasers relative to the wavemaker were obtained by trial and error.

The flow fields were seeded with titanium dioxide particles with diameters of about 1.4 μm and a specific gravity of about 2.5. These particles were chosen because of their high reflectivity to light, low cost and ability to follow the flow, as is demonstrated in the following. The first concern for the motion of the particles is the sinking rate. The particles have an irregular shape, but an order of magnitude for their terminal velocity can be obtained using the Stokes drag law (spherical particles) in the vertical momentum equation for the particle. The resulting terminal velocity is 0.005 mm s^{-1}. Thus, during the time between laser pulses (0.4–0.5 ms), a particle will sink by a distance of only 2% of its diameter. This will have an insignificant effect on the computed velocities. To determine the ability of the particles to follow the fluid motion, the work of Hjelmfelt & Mockros 1966 was used. In this work, the motion of particles of density ratio of 2.65 (which is about the same as that of the current particles) in a turbulent flow was studied theoretically. It was found that the particles would closely follow the fluid if the Stokes number,

$$N_s = \sqrt{\frac{\nu}{\omega d^2}}, \tag{2.1}$$

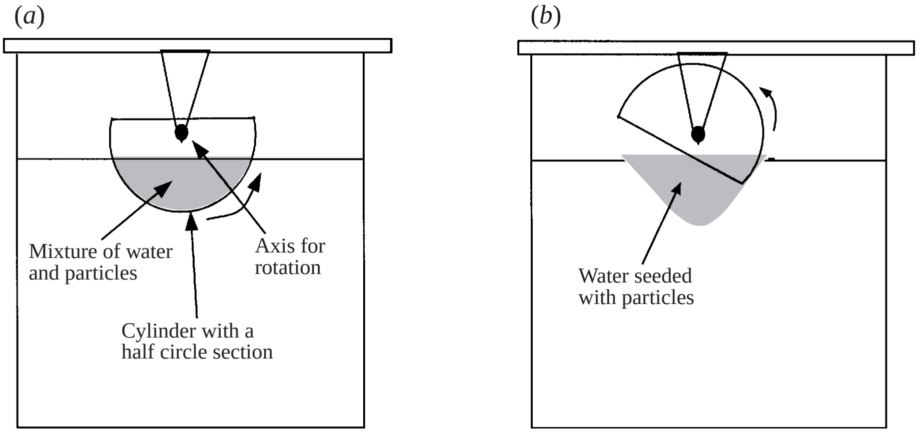

FIGURE 4. Schematic showing particle seeding with a half-cylindrical tank.

is greater than 2, where d is the particle diameter, ν is the kinematic viscosity and ω is the radian frequency of the velocity fluctuations. For the particles used in the present study and with ν taken as $0.013\,\mathrm{cm}^2\,\mathrm{s}^{-1}$, equation (2.1) with $N_s = 2$ predicts that the particles will closely follow the turbulent flow if the frequencies are less than 26 400 cycles per second. The usual range of frequencies for turbulent flows is 1–10 000 cycles per second (Hjelmfelt & Mockros 1966), thus the particles used in the present experiment should follow the turbulent flows quite well.

The particle number density was carefully selected by taking test pictures. In the data reported herein, the particle number density was about 6–10 in a PIV interrogation window (roughly $1\,\mathrm{mm}^2$ in the plane of the light sheet, see below). According to Adrian (1991), this number of particles is sufficient for accurate velocity measurements obtained via the correlation methods described later in this section. At these high particle concentrations, the scattering of light is severe. Thus, if the particles were distributed uniformly throughout the tank, the laser light sheet would be severely attenuated as it travelled through approximately 1.3 m of particle laden water between the glass wall where the laser sheet enters the tank and the measurement area. Also, the individual particles in the light sheet would not be clearly visible to the camera which looks through about 0.35 m of water between the glass wall and the light sheet. Thus, the following local particle seeding method, in which the water along most of the optical paths was free of particles, was used. A half-cylindrical tank was mounted on a rod which was placed above the water surface, as shown in figure 4. Before each experimental run, this seeding tank was placed in the water as shown in figure 4(*a*). The particles were then mixed into the water in the seeding tank. After the turbulent motion in the tank caused by stirring died down, the cylindrical tank was rotated slowly until it was fully out of the water. In this manner, the particle laden water formerly in the cylindrical tank remained fairly stationary in the wave tank (see figure 4*b*). It was found during the experiments that this particle laden volume of water would remain intact for about 45–60 s except that the particles at the water surface would sink about 1 mm, leaving a layer of water with no particles. Since the measurement of the flow velocities near the surface was essential in this research, a very gentle spray of particle laden water was applied at the water surface to bring up the near-surface particle concentration at about 30 s before taking each PIV image. It was found that the small disturbance on the water surface from this spray would quickly die down and had little effect on the wave-breaking pattern.

The shutter on the camera was set to capture two light pulses, one from each laser, on a single negative. As the wave approaches breaking, the fluid velocities in the crest approach and then exceed the wave crest speed (about $1\,\mathrm{m\,s^{-1}}$ relative to a fixed observer). All the fluid particles in the region of interest are moving with relatively high velocity in the direction of wave propagation. Thus, with the camera fixed relative to the laboratory reference frame, there was no directional ambiguity in the particle displacements in the PIV images. With the selected time separation between laser pulses, the displacements between the two images of a single particle were between 12 and 35 pixels on the digitized image. This range of displacements corresponded to roughly 0.5–$1.2\,\mathrm{m\,s^{-1}}$ in the physical flow field and is quite reasonable in view of the wave crest speeds which range from 0.95 to $1.13\,\mathrm{m\,s^{-1}}$.

One PIV picture was taken during each run of the experiment. By moving the camera in small steps along the wave propagation direction and simultaneously increasing the time delay between the beginning of the wavemaker motion and the time at which the PIV image was taken, the evolution of the breaking wave flow field was followed. If the waves in different runs were exactly repeatable, these pictures at different positions would be equivalent to a series of cinematic PIV pictures that followed the flow field in the wave crest. However, the development of the toe and capillary waves, the point in the wave development when the toe begins to move down the wave face, and the details of the development of the ensuing turbulent flow are not identical from run to run. These variations are typical of any unsteady flow that changes from a laminar to turbulent state. Variations in the surface profile histories of the present waves from run to run for a single wavemaker motion were discussed in detail in Duncan *et al.* (1999). The repeatability/variations of the present PIV measurements are addressed to some extent in the results sections of the present paper. However, owing to the experimental difficulties in obtaining the present measurements, the data sets are not as complete as in Duncan *et al.* (1999).

2.3. *PIV image processing*

The PIV images were digitized with a Nikon 3510AF film scanner at a spatial resolution of 125 pixels $\mathrm{mm^{-1}}$. This corresponds to about 60 pixels $\mathrm{mm^{-1}}$ in the plane of the light sheet. With this resolution, each $1.4\,\mu\mathrm{m}$ diameter particle is covered by only 0.08 pixels. However, owing to the point response function of the lens, the diameter of the image of each particle (either calculated via equation (5) in Adrian (1991) or measured from the present images) is about 2 pixels.

Velocities in the flow field were obtained from the PIV images using two-dimensional correlation techniques described in Adrian (1991) and Keane & Adrian (1992). The size of the interrogation window was typically 70×70 pixels. Adjacent windows were overlapped by 50%, resulting in a grid spacing of flow vectors of 0.58 mm measured in the plane of the light sheet. The position of the free surface in each image was determined by eye. We estimate that the accuracy of the free surface location is about half of one interrogation window, 0.58 mm. To obtain the correlation in each window, the direct cross-correlation method was used primarily, though in some cases a two-dimensional auto-correlation method based on a fast Fourier transform (FFT) method was used. Subpixel particle displacement accuracy was achieved by fitting the two-dimensional correlation function with an eighth-order polynomial function. The peak of the polynomial was taken as the correlation peak.

By the above approach, the error in the computed particle displacements was about ± 0.3 pixels which corresponds to an error of $\pm 3\%$ in the fluid velocity measurements. Computed vectors that were obviously in error, were fixed by varying the interrogation window size, using the two-dimensional FFT correlation method, or, in rare instances, by averaging the neighbouring vectors. To obtain the vorticity component normal to the plane of the light sheet the necessary spatial derivatives of the velocity were obtained via first-order differences. The resulting vorticity field was then smoothed with a nearest neighbour filter. The error in the vorticity measurement was estimated to be about 15%. Measurements of the flow field far from the free surface, where there is no vorticity, indicate that the background noise level in a given flow field was at most $25\,s^{-1}$.

In some regions of the flow, particularly near the free surface of the capillary waves and the toe of the breaking region, the shear layers can be very thin. These flow features are typical of all breaking wave flows since masses of water with opposing velocities meet and slide over one another during the breaking process. An example of a PIV image of a shear layer near the toe of a short-wavelength steady breaker can be seen in the PIV images in figure 7 of Lin & Rockwell (1995). As can be seen in the figure, the fluid velocity changes dramatically in magnitude and direction over a distance of less than the typical particle spacing. Thus, in the analysis of these images, the PIV window, which must contains six or more particles, covers a region of widely varying particle displacements. Since the standard PIV algorithms, like the one used here, assume that the velocity in each window is constant, these thin shear layers cause errors in the computed velocities. These problems have been quantified to some extent in the studies of Keane & Adrian (1992) and Cowen & Monismith (1997), which address the effect of a linear shear on the correlation results, and by the study of Adrian (1991), which has shown that correlations in windows with two flow regions separated by a thin shear layer can result in weak double correlation peaks. In the present case, it was decided to obtain PIV images that cover the entire turbulent region at the crest of the wave in order to obtain the overall flow patterns and measure global quantities such as the total circulation and the maximum velocity at a given instant in time. Given the large scale of the flow and therefore the region covered by the PIV images, great effort was expended to achieve the smallest possible interrogation window. However, it is realized that the most intense shear layers are not resolved properly and the velocity and vorticity fields in these regions are smoothed in some complex way.

2.4. *Experimental conditions*

Four different breaking waves were studied (see table 1). The mean wave packet frequencies ($f_0 = 1.42$, 1.26 and 1.15 Hz) were the same as those used in Duncan *et al.* (1999). At each frequency, one or two dimensionless wavemaker amplitudes, A/λ_0 (where A is the overall amplitude of the wavemaker motion (see Duncan *et al.* 1999 equation (2.1)) and $\lambda_0 = g/(2\pi f_0^2)$ where g is the acceleration due to gravity), were chosen. These amplitudes are slightly different from those in Duncan *et al.* (1999). The time delay between the laser pulses in the PIV images is also given in the table.

3. Results and discussion for the 1.42 Hz wave

The flow fields for the 1.42 Hz wave for times before the toe begins to move down the wave face are presented and discussed in § 3.1 and the flow fields for subsequent times are presented and discussed in § 3.2. Each flow field measurement is referenced by the distance (X_{wm}) from the back face of the wavemaker to the wave crest at the time that the PIV image was taken. In the discussion, the upstream and downstream directions are defined considering the mean horizontal flow component relative to the

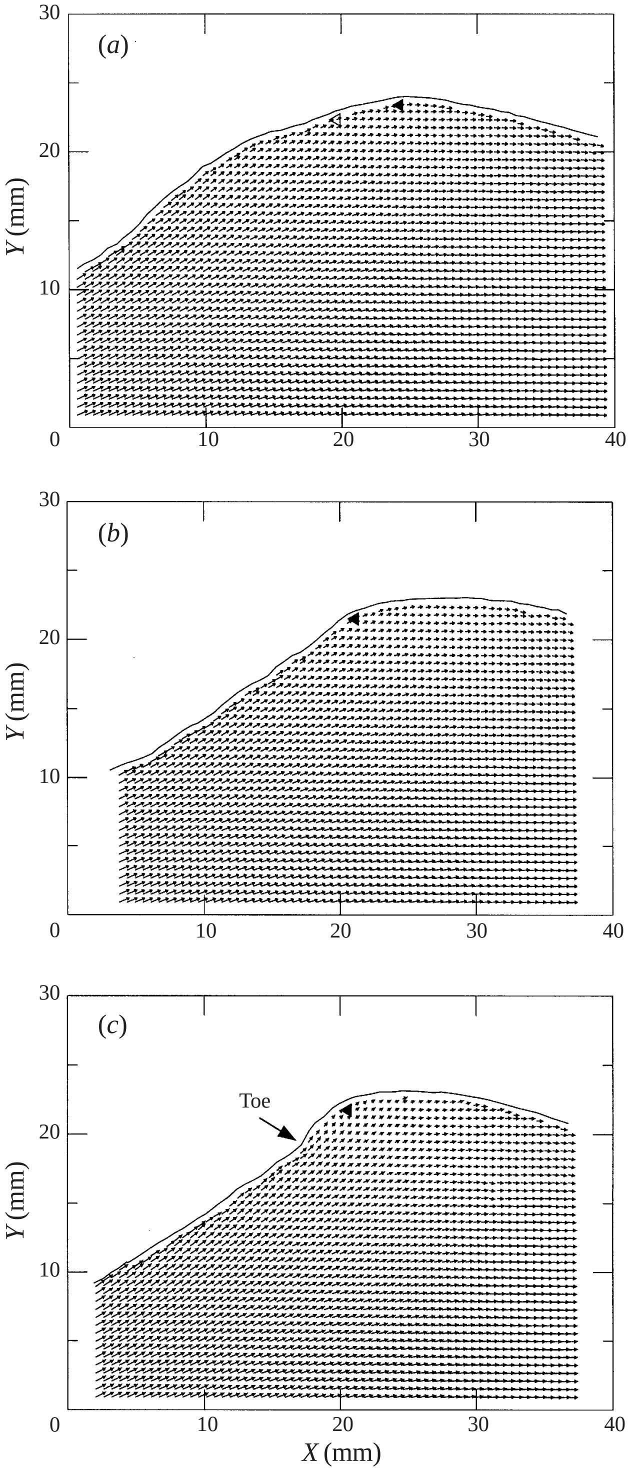

FIGURE 5 (*a*–*c*). For caption see facing page.

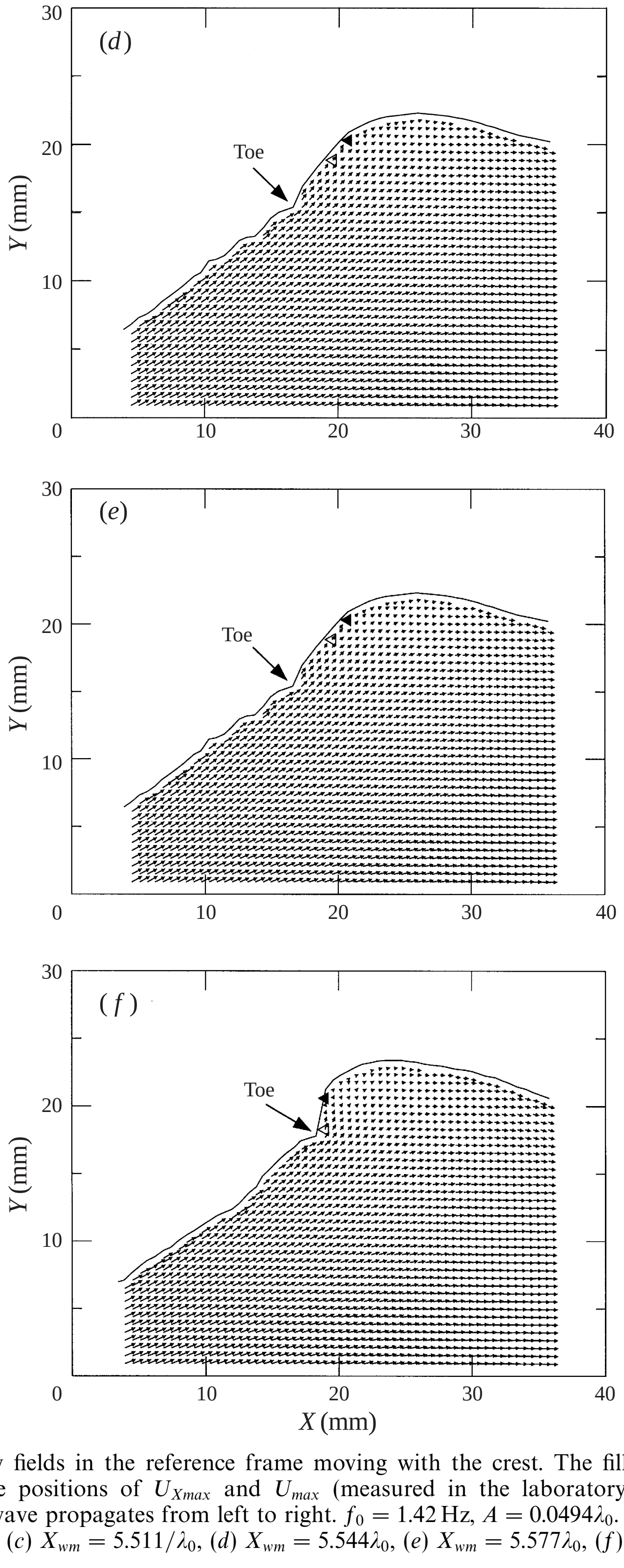

FIGURE 5. Velocity fields in the reference frame moving with the crest. The filled and the empty triangles mark the positions of U_{Xmax} and U_{max} (measured in the laboratory reference frame), respectively. The wave propagates from left to right. $f_0 = 1.42$ Hz, $A = 0.0494\lambda_0$. (*a*) $X_{wm} = 5.445\lambda_0$, (*b*) $X_{wm} = 5.478\lambda_0$, (*c*) $X_{wm} = 5.511/\lambda_0$, (*d*) $X_{wm} = 5.544\lambda_0$, (*e*) $X_{wm} = 5.577\lambda_0$, (*f*) $X_{wm} = 5.609\lambda_0$.

crest. Thus, downstream is to the right in the flow field plots like that shown in figure 5. On the other hand, for those velocities that are given relative to the laboratory reference frame, a positive x-component is defined as in the direction of the wave phase velocity.

3.1. *The crest flow field evolution before the toe begins to move.*

3.1.1. *Results*

Figure 5 shows a series of flow fields of the 1.42 Hz wave (see table 1 for wave generation parameters) for times before the toe begins to move down the wave face. The area covered in each flow field is approximately 4 cm×3 cm, and the velocities are shown for a viewer moving with the crest. The spatial coordinates on the PIV images are not referenced to a fixed zero point in laboratory coordinates. Thus, the velocities at specific X-Y locations in one flow field cannot be compared directly to the velocity at the same X-Y location in a similar flow field. As was explained at the end of § 2.2, each flow field was obtained in a separate experimental run. Flow fields from various stages of the breaking process were obtained by varying simultaneously the camera position and the time at which the PIV image was taken relative to the start of the wavemaker motion. The total camera position difference from figure 5(*a*) to figure 5(*f*) is $\Delta X_{wm} = 12.70\,\text{cm}$, which corresponds to a time interval of 0.134 s given the crest speed of $U_{crest} = 94.65\,\text{cm s}^{-1}$ (see Duncan *et al.* 1999, table 1).

By examination of the flow fields in figure 5 and the corresponding surface profile images (see figure 3 and the discussion in § 2.2), it is possible to relate each of the measured flow fields to the various stages in the breaking process as described in Duncan *et al.* (1999). The surface profile images were also used to determine the position of the toe in each flow field and these positions are marked in each figure. The breaking stages shown in the flow fields in figure 5 are as follows. The crest is just becoming asymmetric in figure 5(*a*) and develops into the asymmetric form in figure 5(*b*). In figure 5(*c*), there is a bulge forming at the forward face of the crest. From figures 5(*c*) to 5(*f*), the bulge becomes more pronounced. In subsequent flow fields (see § 3.2), the bulge begins to flatten and the toe moves relative to its initial position.

In figure 5, the positions of the maximum horizontal particle speeds (u_{max}) and the positions of the maximum particle speeds ($|\boldsymbol{u}|_{max}$) are marked by filled triangles and empty triangles, respectively; both are measured relative to the laboratory reference frame. If no empty triangle appears in a figure, then the two triangles are at the same position. In all cases after the toe formation, u_{max} and $|\boldsymbol{u}|_{max}$ are located between the crest and the toe. The plots show that u_{max} is near the top of the crest in figure 5(*a*) and a little forward of the crest in all later figures, while $|\boldsymbol{u}|_{max}$ is forward of the crest in all cases and is either at the same position as the u_{max} (figures 5*b* and 5*c*) or at a position a ahead of u_{max} (figures 5*d*, 5*e* and 5*f*).

The scaled maximum horizontal particle speeds, u_{max}/U_{crest}, and the scaled fluid velocity at the measurement point closest to the toe, $\boldsymbol{u}_{toe}/U_{crest}$, in figure 5 are shown in table 2. The value of u_{max}/U_{crest} increases from 0.741 in figure 5(*a*) to 0.948 in figure 5(*f*); however, the value does not increase monotonically from figure to figure. The randomness in these values probably results from the differences in the development of the wave from run to run. In spite of this randomness, the data indicate that before the toe-motion phase of the wave development, u_{max} approaches but does not go above the crest phase speed. The fluid velocity at the toe in the reference frame of the crest is in the upslope direction with magnitudes of about 0.07.

Figure	X_{wm}/λ_0	u_{max}/U_{crest}	$\boldsymbol{u}_{toe}/U_{crest}$
5(*a*)	5.445	0.741	–
5(*b*)	5.478	0.764	–
5(*c*)	5.511	0.886	(0.673, 0.192)
5(*d*)	5.544	0.869	(0.636, 0.259)
5(*e*)	5.577	0.892	(0.713, 0.200)
5(*f*)	5.609	0.948	(0.665, 0.186)

TABLE 2. Maximum horizontal component of fluid velocity (u_{max}) and fluid velocity at the toe ($\boldsymbol{u}_{toe}$) relative to the laboratory reference frame for the velocity fields shown in figure 5. U_{crest} is the phase speed of the wave crest. $f_0 = 1.42$, $A = 0.0494$.

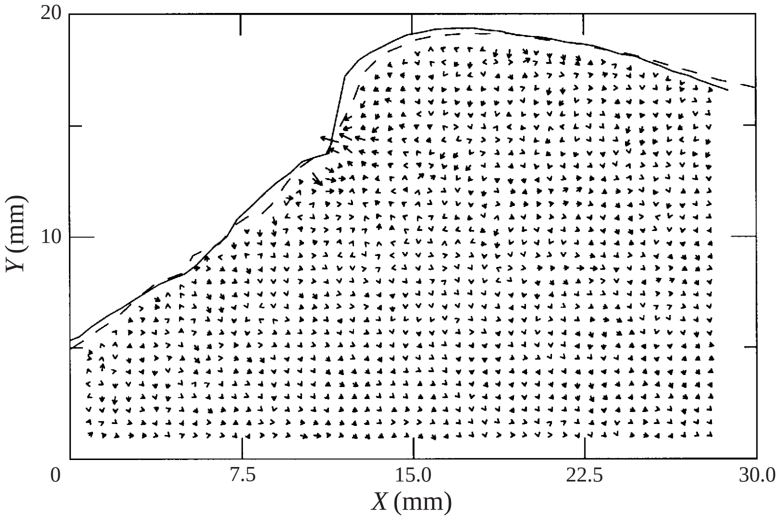

FIGURE 6. Velocity difference between the flow fields in figures 5(*f*) and 5(*e*). The time difference between these two figures was 27 ms. There are significant velocity differences near the toe.

3.1.2. *The nature of the flow*

Two physical mechanisms could be responsible for the shape of the crest before the toe motion begins. In the first mechanism, the bulge is a mass of fluid which has separated from the underlying flow and exists as a weak roller. In this case, the toe would be the leading edge of this mass of fluid and the dividing streamline between the underlying flow and the bulge would begin somewhere near the toe. The fluid velocities relative to the wave crest would be directed downslope (upstream) near the free surface of the bulge. In the second mechanism, the bulge, toe and capillary waves are a wavelike phenomenon similar to the capillary jump theory suggested by Longuet-Higgins (1996). In this case, the fluid particle speed in the bulge and around the toe would follow the contour of the free surface and always have a component of downstream flow relative to the crest. The flow fields presented in figure 5 support the description of the crest profile features as a wavelike phenomenon; the particle speeds are all directed downstream and there is no evidence of a separated roller under the bulge.

Figure 6 shows the velocity differences between figures 5(*f*) and 5(*e*). Because the x-y positions of the velocity vectors in figures 5(*f*) and 5(*e*) are not the same (see

Figure	X_{wm}/λ_0	u_{max}/U_{crest}	$\boldsymbol{u}_{max}/U_{crest}$	u_s/U_{crest} see (3.2)	$\boldsymbol{u}_{toe}/U_{crest}$
7	5.642	0.927	(0.927, 0.139)	−0.133	(0.681, 0.230)
8	5.642	0.994	(0.977, 0.309)	−0.174	(0.749, 0.283)
9	5.659	1.15	(1.150, 0.0138)	0.123	(0.665, 0.298)
11	5.675	1.31	(1.310, −0.403)	0.470	(0.764, 0.128)
12	5.724	1.17	(1.170, 0.003)	0.146	(0.788, 0.260)
14(*a*, *b*)	5.741	1.26	(1.260, −0.162)	0.306	(0.409, 0.288)
14(*c*, *d*)	5.741	1.30	(1.300, 0.000)	0.260	(0.430, 0.296)

TABLE 3. Maximum horizontal particle speed (u_{max}), maximum particle velocity ($\boldsymbol{u}_{max}$), estimate of the downslope component of $\boldsymbol{u}_{max}$ (u_s), and particle velocity at the toe ($\boldsymbol{u}_{toe}$) for breaking stages after the toe begins to move relative to the wave crest. The velocities u_{max}, $\boldsymbol{u}_{max}$, and $\boldsymbol{u}_{toe}$ are given in the laboratory reference frame while u_s is given relative to the wave crest. $f_0 = 1.42$, $A = 0.0494$.

the discussion at the beginning of this subsection), one figure was moved by small offsets in both the x- and y-directions until the two surface profiles nearly matched before the velocity differences were computed. As can be seen from figure 6, while in most of the region near the crest the difference flow vectors are nearly zero, there is a significant difference flow near the toe. Since the lengthscale (radius of curvature) of the toe is small (1–5 mm), capillary forces should play an important role in the development of the flow in this region.

In analysing the above difference flow, it was realized that in the vicinity of the toe, where the velocity varies rapidly with position, the results might be sensitive to errors in the position offset values between the two flow fields. Thus, in an attempt to estimate the reliability of the difference flow vectors near the toe, difference flow vectors were also computed between one of the flow fields and the same flow field after a small spatial offset. The resulting ‘self’ difference flow vectors were compared to those in figure 6; it was found that the errors caused by errors in the offset values are not significant.

3.1.3. *Vorticity*

The vorticity component normal to the plane of the light sheet was computed from each of the flow fields in figure 5. No vorticity magnitudes higher than the background noise level were found. In contrast to this finding, Longuet-Higgins (1992) predicted that the capillary waves upstream of the toe would generate significant vorticity at similar stages of the wave motion. In order to examine this discrepancy, the thickness (δ_c), mean vorticity ($\overline{\varpi}_\infty$), and induced velocity ($\overline{u}_0$) of the boundary layer under the capillary waves as predicted by the theory were computed given the data from Duncan *et al.* (1999) for the capillary wavelength amplitude and duration (see Appendix A). The results are $\delta_c = 0.51\,\mathrm{mm}$, $\overline{\varpi}_\infty = 181.6\,\mathrm{s}^{-1}$, and $\overline{u}_0 = 7.6\,\mathrm{cm\,s}^{-1}$. Though the present experimental techniques are capable of measuring the magnitudes of both $\overline{u}_0$ and $\overline{\varpi}_\infty$ with sufficient accuracy (see § 2.3), the spatial resolution of the measurements, 0.58 mm, is not sufficient to resolve the boundary layer. Thus, the predictions of Longuet-Higgins (1992) cannot be confirmed. In order to obtain, say, four velocity measurements within the boundary layer, the present PIV window size would have to be reduced by a factor of about 0.25. There are many obstacles to obtaining this improved spatial resolution in the present large-scale flow.

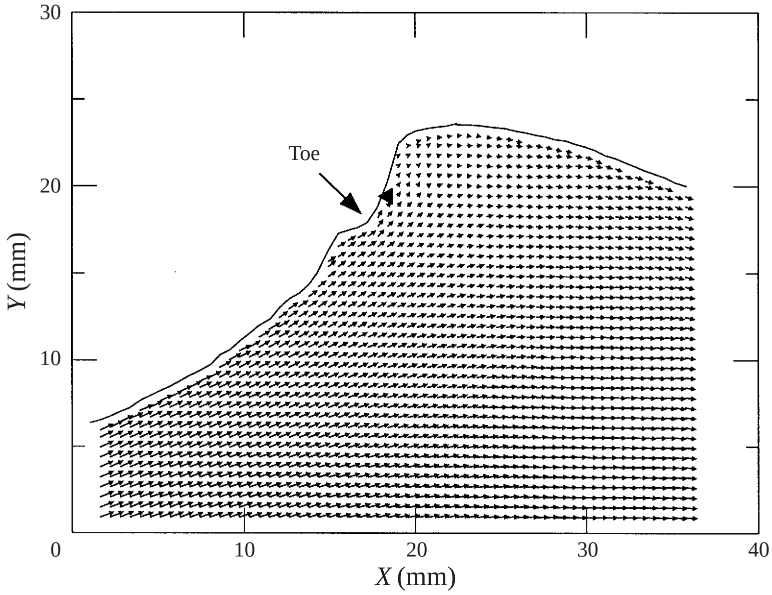

FIGURE 7. Velocity field at $X_{wm} = 5.642/\lambda_0$ in the reference frame moving with the crest. $f_0 = 1.42$ Hz, $A = 0.0494\lambda_0$. See figure 5 for details.

3.2. *The crest flow field evolution after the toe begins to move*

3.2.1. *Results*

The velocity and vorticity fields at breaking stages after the toe starts to move down the wave face are presented (figures 7–14). Values of u_{max}, $\boldsymbol{u}_{max}$ and $\boldsymbol{u}_{toe}$ for each flow field are given in table 3. In the flow fields depicted in figures 7 and 8, which were measured on separate experimental runs but at the same position and delay time, the toe motion has just begun. The differences between these flow fields are evidence of the randomness in the wave development during this phase of the breaking process. As indicated by the toe positions marked in each figure, the toe has barely started to move in figure 7, whereas in figure 8 the toe has been moving for a slightly longer time. The maximum horizontal components of the velocity in figures 7 and 8 are $0.927U_{crest}$ and $0.994U_{crest}$, respectively. There is no vorticity above the noise level in the velocity field given in figure 7, whereas the velocity field in figure 8 contains a small patch of positive vorticity near the toe with a maximum contour level of $100\,\mathrm{s}^{-1}$, see figure 8(*b*). All subsequent velocity fields show substantial positive vorticity; no negative vorticity was measured in any flow field.

As the breaking process continues, the surface profile measurements reported in Duncan *et al.* (1999) indicate that the toe accelerates quickly and then reaches a constant speed for a short time. The velocity and vorticity fields for $X/\lambda_0 = 5.659$ (1.27 cm farther from the wavemaker than the flow fields in figures 7 and 8) are given in figures 9(*a*) and 9(*b*), respectively. Examination of the original images indicates that the toe is moving rapidly down the wave face at this point in the wave development and that there are ripples between the toe and the crest. The flow vectors near the toe are still in the downstream direction in the reference frame moving with the crest. However, as marked on figure 9(*a*), there is a point on the surface where the flow reverses, i.e. the flow vectors are in the downstream direction at positions upstream of this point and in the upstream direction at positions downstream of this point. A

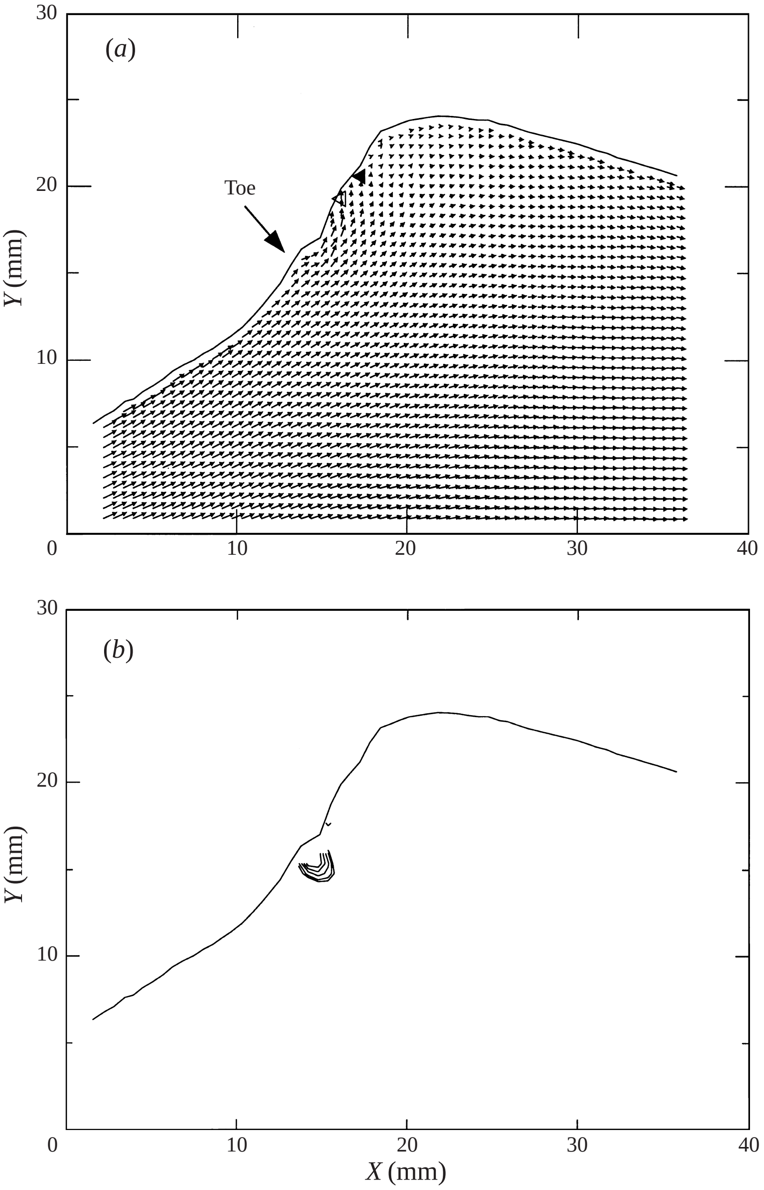

Figure 8. Flow measurements at $X_{wm} = 5.642\lambda_0$. (*a*) Velocity field in the reference frame moving with the crest. (*b*) Vorticity. Contour levels are 30, 40, 60, 80, 100 (s^{-1}). $f_0 = 1.42\,\mathrm{Hz}$, $A = 0.0494\lambda_0$. See figure 5 for details.

strong shear layer starts at this flow reversal point and stretches almost horizontally downstream into the flow field. Figure 10 shows the same velocity field as in figure 9(*a*) but in the reference frame that is moving at a speed of $0.667U_{crest}$. The shear layer can be more clearly identified in this figure as can a strong kinetic energy concentration at the forward face of the crest. The maximum horizontal particle speed is $1.15U_{crest}$ in the laboratory reference frame at a position about halfway between the crest and the toe. The corresponding vorticity plot in 9(*b*) shows a vortical region composed primarily of a single eddy. This region extends from the surface a little downstream

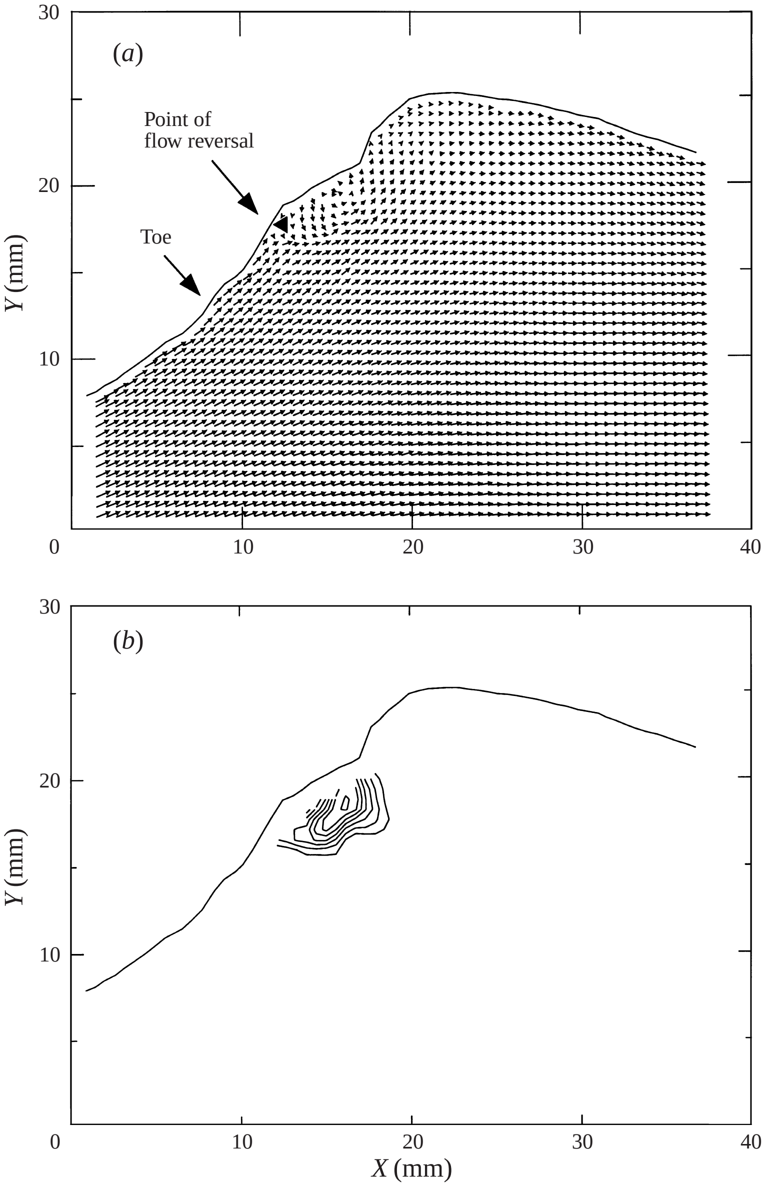

FIGURE 9. As figure 8 but at $X_{wm} = 5.659\lambda_0$. Minimum and incremental levels of vorticity are $\omega_{min} = 40\,\mathrm{s}^{-1}$ and $\Delta\omega = 40\,\mathrm{s}^{-1}$. See figure 5 for details.

of the toe and just upstream of the flow reversal point to about halfway between the toe and the crest. Both the peak value ($240\,\mathrm{s}^{-1}$) and the spatial extent of the vorticity are increased considerably compared to figure 8(*b*).

Figures 11(*a*) and 11(*b*) ($X_{wm} = 5.675\lambda_0$) show the velocity and vorticity fields, respectively, for a breaking stage 1.24 cm farther from the wavemaker than the flow field shown in figure 9. The maximum horizontal particle speed has increased to $1.31U_{crest}$ and is located on the surface about midway between the toe and the crest. The vortical region extends from the free surface near the toe to just upstream of the crest and is longer along the free surface and deeper below the free surface than the

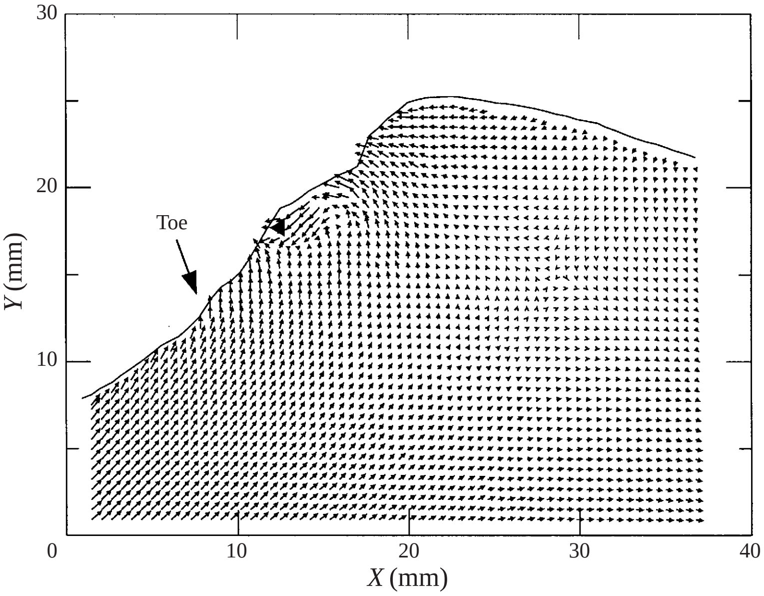

FIGURE 10. Velocity field at $X_{wm} = 5.659\lambda_0$ in the reference frame moving at $0.333 \times U_{crest}$. See figure 5 for details.

vortical region in figure 9(*b*). There are three vorticity peaks in figure 11(*b*) and the maximum vorticity is $280\,\mathrm{s}^{-1}$, a little higher than that of figure 9(*b*). The eddy with the largest vorticity peak is found farther below the free surface than the other two eddies and considerably farther downstream from the toe.

The velocity and vorticity fields shown in figures 12(*a*) and 12(*b*), respectively, were taken at $X_{wm} = 5.724\lambda_0$. The flow has evolved considerably from that depicted in figure 11 which was taken 3.79 cm closer to the wavemaker. The maximum horizontal flow speed in figure 12(*a*), $1.17U_{crest}$, is lower than that in the previous flow field. The velocity field is shown again in figure 13 in a reference frame moving at a speed of $0.667U_{crest}$ in order to better show the vortices and shear layers in the flow. A large flow structure exists just below the filled triangle in the figure. In this flow structure, the fluid moves up from the inner flow to the surface (right of the triangle in the figure) and from the surface to the inner flow (left of the triangle in the figure). This flow structure shows the exchange fluid between the surface and the underlying flow. The vortical region in figure 12(*b*) extends along the surface from the toe to the crest covering a length of about 4 cm and reaches a maximum depth below the free surface of about 0.7 cm. This region contains many local peaks and the maximum vorticity magnitude is $240\,\mathrm{s}^{-1}$.

At $X_{wm} = 5.741\lambda_0$, 1.31 cm farther from the wavemaker than the previous flow field measurement, two realizations of the velocity and vorticity fields are given in figures 14(*a, b*) and 14(*c, d*). The maximum components of horizontal fluid velocity in the two figures are $1.26U_{crest}$ and $1.30U_{crest}$. As in figure 12, the vortical regions extend from the toe to the crest in both cases and contain a number of local vorticity peaks. The maximum vorticity peak is $280\,\mathrm{s}^{-1}$ in figure 14(*a, b*) and $320\,\mathrm{s}^{-1}$ in figure 14(*c, d*).

3.2.2. *Discussion*

Between figures 7 and 14, a vortical region is created that reaches a maximum length of about 4 cm and a typical depth of about 0.8 cm below the free surface.

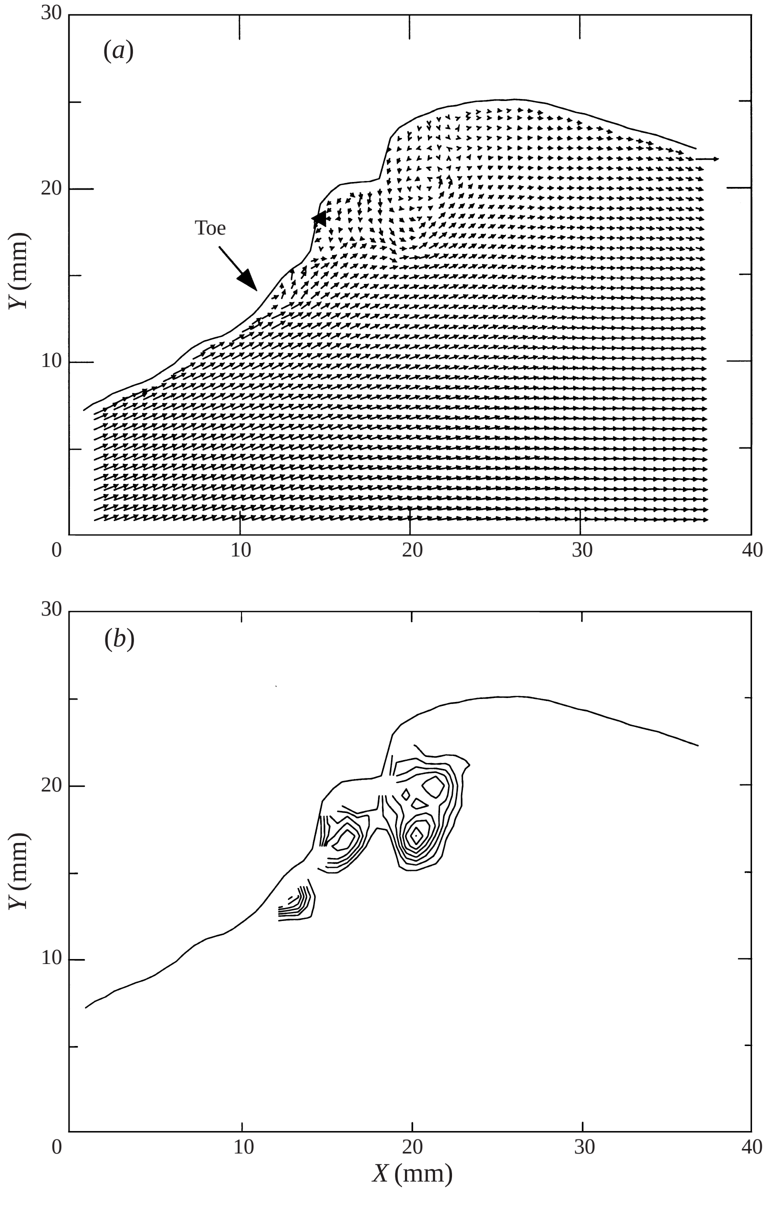

FIGURE 11. As figure 9 but at $X_{wm} = 5.675\lambda_0$.

During this time period, the wave crest moves a distance of 7.7 cm. The vorticity first appears just downstream of the toe and progressively extends from the toe as the breaking process continues. The maximum vorticity level increases rapidly when the toe first starts to move, but then attains a fairly constant level while the area of the vortical region grows. As will be seen in the next section, the total circulation grows dramatically during this phase of the breaking process.

The velocity and vorticity patterns shown in figures 12 to 14 are qualitatively similar to those given in figure 6 of Lin & Rockwell (1995) for a steady breaker generated by a submerged hydrofoil. In both cases, the vorticity is distributed in a thin layer

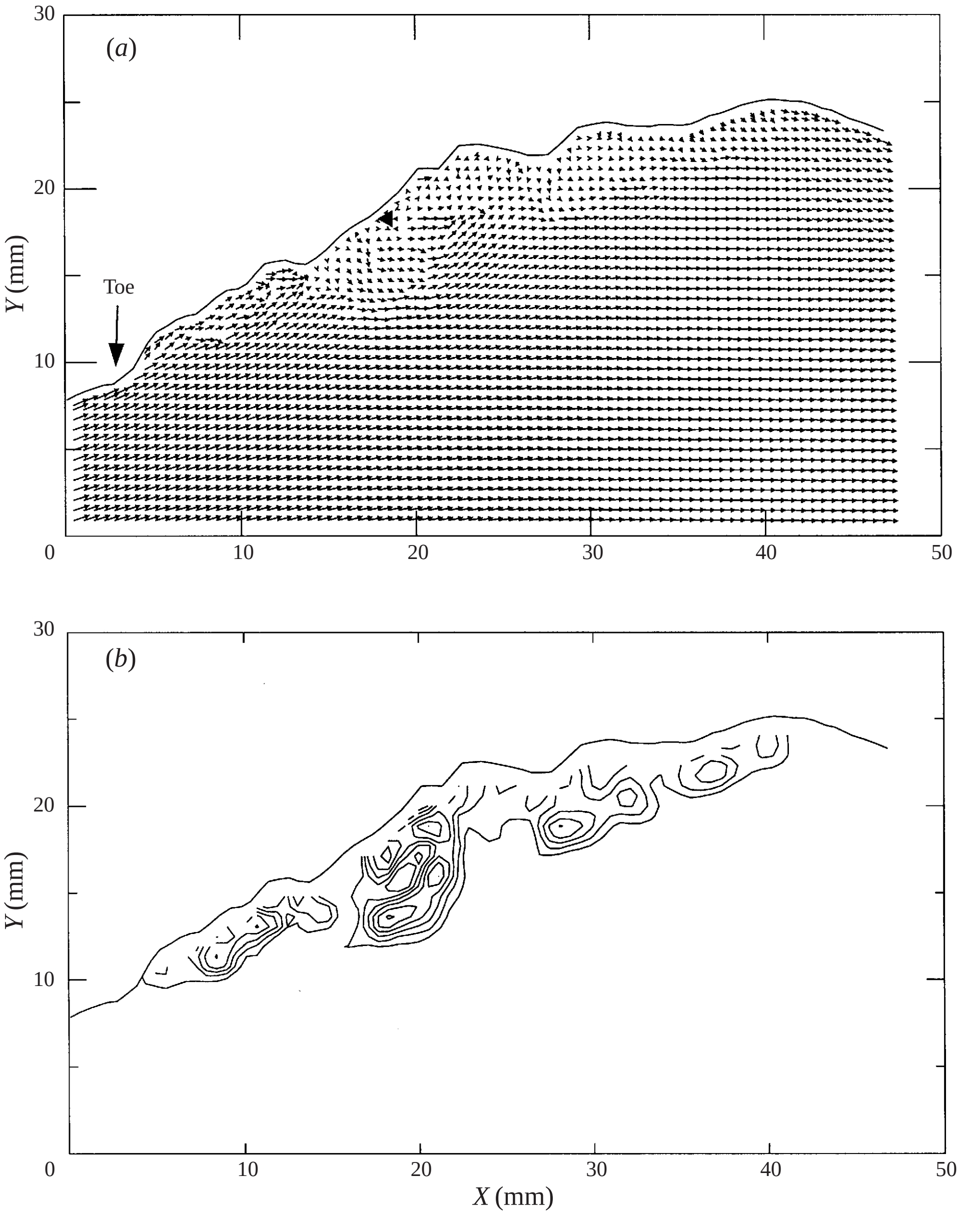

FIGURE 12. As figure 9 but at $X_{wm} = 5.724\lambda_0$.

beneath the free surface starting at the toe. In the steady breaker case, the vorticity distribution continues downstream into the wake, while in the present case, the vorticity is confined to a short streamwise region owing to the short time over which it is generated. In both cases, the highest vorticity values appear just downstream of the toe. The typical maximum vorticity levels in the steady breakers are $282\,\mathrm{s}^{-1}$ and $456\,\mathrm{s}^{-1}$ for the $F_r = 0.49$ and 0.56 cases, respectively, while in the present case the maxima range from $240\,\mathrm{s}^{-1}$ to $320\,\mathrm{s}^{-1}$ (see figures 12 to 14). The similarity between the maximum vorticity levels in the two experiments is at first surprising given the very different phase speeds of the breakers: $42.2\,\mathrm{cm\,s}^{-1}$ ($F_r = 0.49$) and $48.2\,\mathrm{cm\,s}^{-1}$

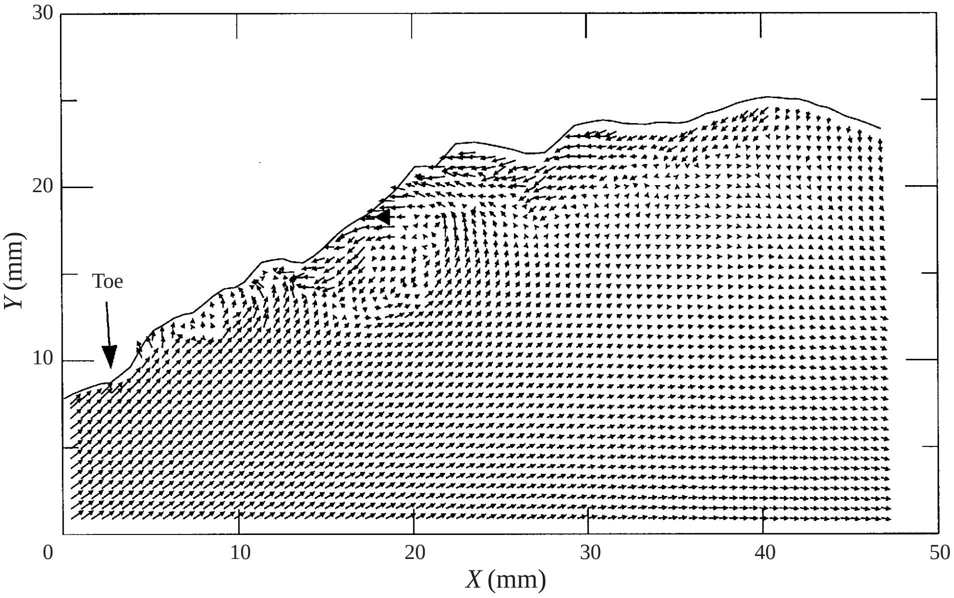

FIGURE 13. Velocity field at $X_{wm} = 5.724\lambda_0$ in the reference frame moving at $0.333 \times U_{crest}$. See figure 5 for details.

($F_r = 0.56$) for Lin & Rockwell (1995) and 94.5 cm s^{-1} in the present case (see table 1 of Duncan *et al.* 1999). However, it is hypothesized that the vorticity levels are more closely related to the velocity difference between the fluid in the breaking region and that in the undisturbed flow near the toe than the wave speed. A comparison of the velocity differences in the two experiments is given below. (The possibility exists that the spatial resolution of the PIV measurements influences the maximum vorticity levels obtained in both the present and Lin & Rockwell (1995)'s experiment. However, it is not possible to test this hypothesis.) In Lin & Rockwell (1995), the toe of the breaker is near the trough and the undisturbed flow speed near the toe is greater than the mean flow speed. Estimates of the lengths of the velocity vectors in figures 6(*a*) and (*b*) of Lin & Rockwell (1995) indicate that the surface velocities just upstream of the toe are 51 and 82 cm s^{-1} for the breakers with phase speeds of 42.2 and 48.3 cm s^{-1}, respectively. For these steady breakers, the fluid speeds in the breaking zone are approximately zero so the velocity difference is equal to the values given above. In figures 12 to 14 of the present work, the toe is well above the mean water level and the typical fluid velocity in the undisturbed water near the toe is about 45 cm s^{-1}. Since the breaking region is growing in the downslope direction, the fluid velocities in this region are typically in the downslope direction relative to the crest. Maximum values of this flow speed range from 0.0 to $0.3U_{crest}$ (see table 4) so a typical value is about $0.15U_{crest} = 14$ cm s^{-1}. The difference in velocity between the underlying flow and the flow in the breaking region is thus about 59 cm s^{-1}. This value is intermediate between the values found in the two flow conditions of Lin & Rockwell (1995).

Given that this is a homogeneous incompressible flow, it is obvious that the vorticity enters the flow from the free surface. The progressive extension of the vortical region from the toe toward the crest in figures 7 to 14, is consistent with the notion that the source of the vorticity is located near the toe; however, the

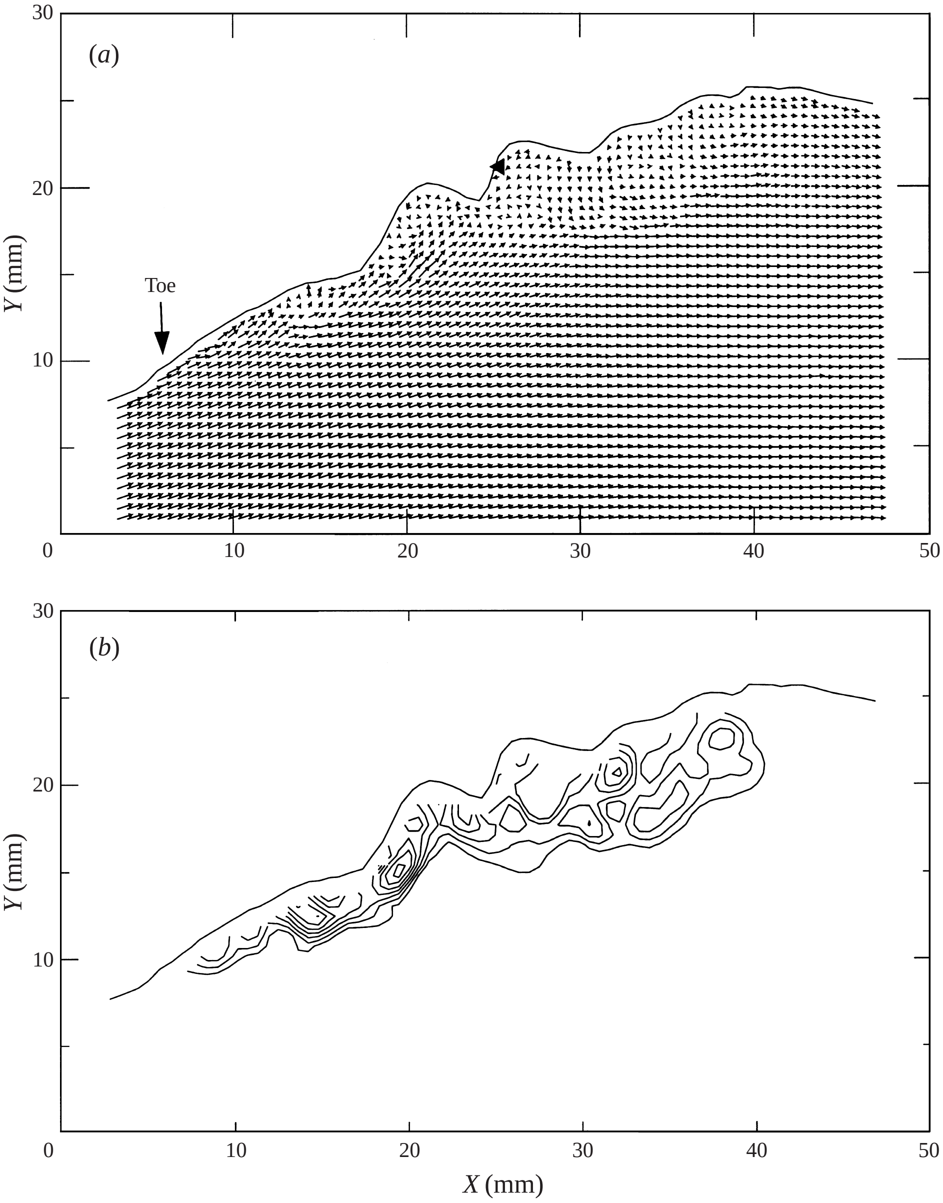

FIGURE 14 (*a, b*). For caption see facing page.

vorticity generation mechanism is difficult to determine. The possibility that, in the early stage of the toe motion, the vorticity is generated by capillary waves upstream of the toe can be addressed in the same manner as in § 3.1 for times before the toe motion began. In Duncan *et al.* (1999), the capillary characteristics were also measured between the time that the toe motion begins and the time when, owing to three dimensionality of the flow, the measurements are no longer feasible (a duration of about 0.015 s). This covers the flow fields in figures 7 to 9 in the present paper. In Appendix A, it is found that the theory predicts a boundary-layer thickness of $\delta_c = 0.6$ mm, a velocity perturbation of $\overline{u}_0 = 64.2\,\mathrm{cm\,s^{-1}}$ and $\overline{\omega}_\infty = 2092\ \mathrm{s^{-1}}$.

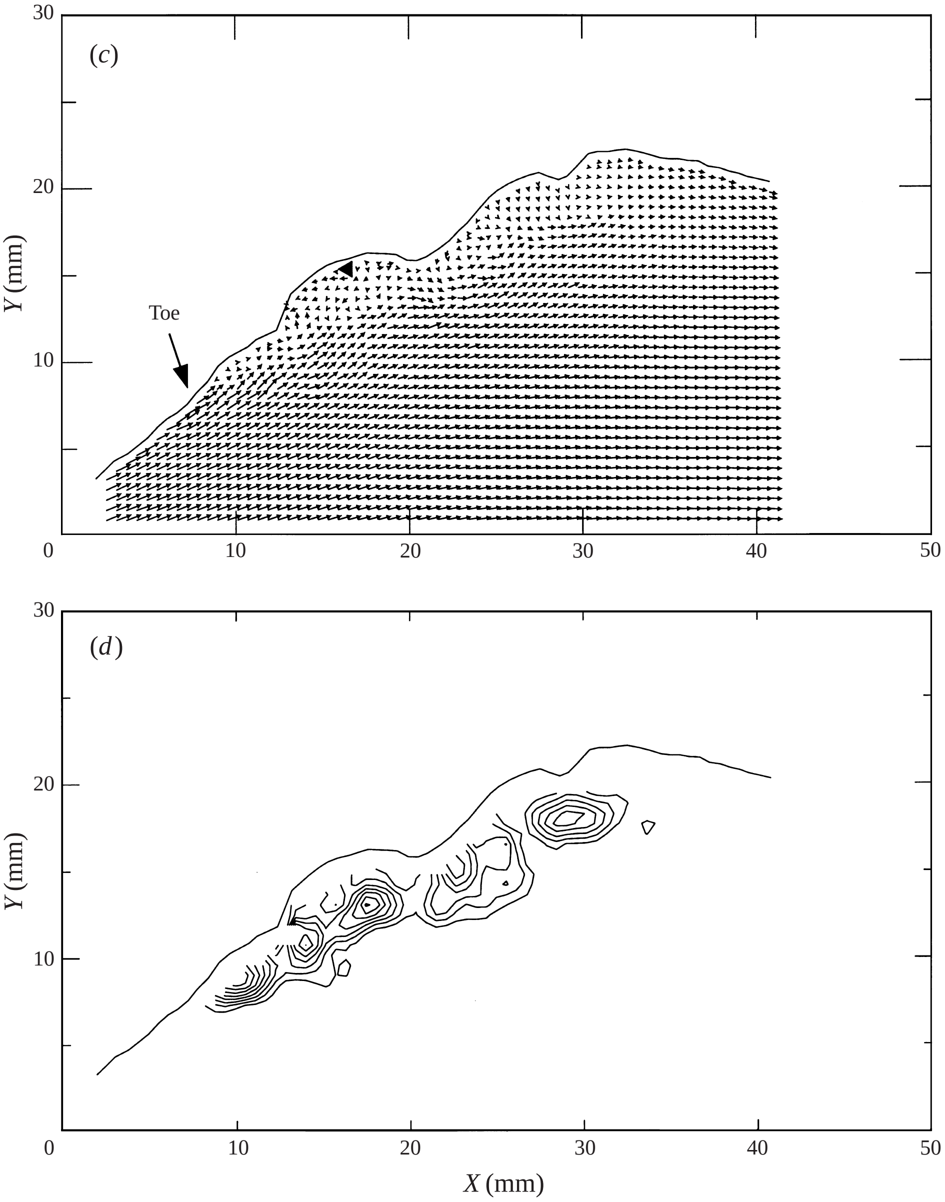

FIGURE 14. As figure 9 but at $X_{wm} = 5.741\lambda_0$. Two realizations are shown.

Again the the boundary layer is too thin to be resolved by the present measurement techniques.

A second mechanism for the generation of the vorticity concerns the possibility of flow separation. In this mechanism, the beginning of toe motion might signal the beginning of the separation of fluid in the bulge from the underlying flow. This process might be initiated at the toe by the boundary layer of the capillary waves and/or the difficulty that the flow has in negotiating the turn around the toe when the curvature at this point reaches a critical value. In order to determine the vorticity flux at the free surface upstream of the toe, we might consider using the equation presented in Rood (1994), Rood (1995) and Gharib & Weigand (1996):

$$\nu \left(\frac{\partial \omega_z}{\partial n} \right)_{n=0} = -\frac{\partial u_s}{\partial t} - g \cos\theta - \frac{1}{2}\frac{\partial u_s^2}{\partial s}, \tag{3.1}$$

where the left-hand side is the vorticity flux, s and n are curvilinear coordinates tangent to and perpendicular to the free surface, respectively, ω_z is the component of vorticity normal to the plane of the light sheet, θ is the angle between s and the horizontal, and u_s is the velocity component parallel to s. Of course, given the ability to measure the terms on the right-hand side, equation (3.1) could be used to determine the vorticity flux in capillary waves too. Dabiri & Gharib (1997) used equation (3.1) without the first term on the right-hand side to calculate the vorticity flux in a short-wavelength quasi-steady breaker found downstream of a screen in a channel flow. In the present work, the flow is highly unsteady so the first term on the right-hand side, which cannot be measured without cinematic PIV images, is likely to be important. Thus, the evaluation of the vorticity flux equation will not be possible until techniques to obtain temporally and spatially resolved cinematic PIV images that can be used in the present large-scale flow become available.

The values of u_{max}, $\boldsymbol{u}_{max}$, and $\boldsymbol{u}_{toe}$ given in table 3 for each flow field show some interesting features. First, the maximum horizontal particle speeds are close to but a little less than U_{crest} as the toe motion begins and then quickly increase to values as high as $1.31U_{crest}$. The concept of incipient breaking occurring when the particle velocity at the crest reaches the wave phase speed was first used by Stokes (1847) in analysing steady, infinite wavetrains without surface-tension effects. For those waves the crest becomes pointed when the incipient breaking condition is reached. This simple breaking criterion works fairly well in the present surface-tension dominated, asymmetric waves. The x-components of the particle velocities near the toe, which range from 0.409 to 0.788 U_{crest}, are still significantly less than the phase speed of the toe, i.e. the horizontal particle velocity is in the downstream direction relative to the crest. If a stagnation point does exist in the vicinity of toe, it must be located closer to the free surface than can be measured with the present PIV technique. Finally, the maximum particle velocity can be compared to the toe velocity as measured from the surface profile histories presented in Duncan *et al.* (1999). In those measurements it was found that the toe moved relative to the wave crest with a speed of $0.25U_{crest}$. The surface slope upstream of the toe varies in time during this phase of breaking, but if we take a typical value of about 30°, then the downslope component of the maximum particle velocity relative to the wave crest is

$$u_s = (u-1)\cos(30^\circ) - v\cos(60^\circ), \tag{3.2}$$

where u and v are the vertical and horizontal components of $\boldsymbol{u}_{max}$. The values of u_s are given in table 4. At the beginning of the toe motion phase, $X_{wm} = 5.642\lambda_0$, u_s is upslope. However, at later times, it is in the downslope direction and ranges in magnitude from $0.123U_{crest}$ to $0.470U_{crest}$, i.e. the same order as the downslope toe speed.

4. Comparison of breaking properties for waves of different frequencies

In the present section, u_{max}, the total circulation (Γ) and the instantaneous flow fields for the three wave frequencies are compared. The scaled maximum horizontal velocity component, u_{max}/U_{crest}, is plotted versus X_{wm}/λ_0 in figure 15. The data for the

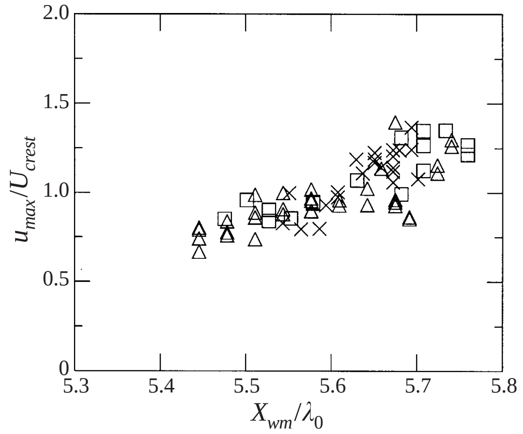

FIGURE 15. Comparison of the scaled maximum horizontal component of the fluid particle velocity, u_{max}/U_{crest}, (relative to the laboratory reference frame) versus X_{wm}/λ_0 for three wave frequencies. ×, $f_0 = 1.15$ Hz; □, $f_0 = 1.26$ Hz; △, $f_0 = 1.42$ Hz.

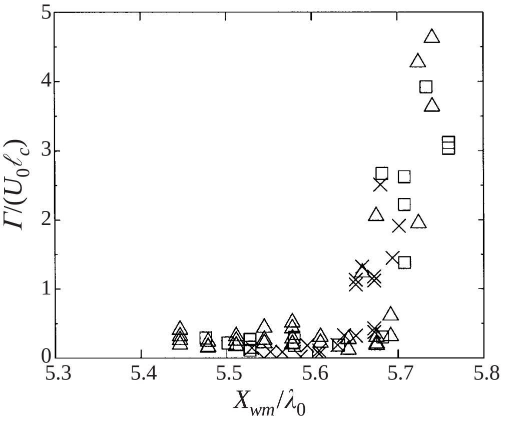

FIGURE 16. Comparison of scaled circulation, $\Gamma/(U_0\ell_c)$, versus X_{wm}/λ_0 for three wave frequencies. ×, $f_0 = 1.15$ Hz; □, $f_0 = 1.26$ Hz; △, $f_0 = 1.42$ Hz.

wave generated with the largest wavemaker amplitude ($f_0 = 1.15$ Hz, $A = 0.0502\lambda_0$) were shifted by $0.1\lambda_0$ to the right in the figure to account for the fact that this wave starts to break a little closer to wavemaker than the other three waves. As can be seen from the figure, the magnitude of u_{max} stays under but quite close to U_{crest} from $X_{wm} = 5.50\lambda_0$ to about $5.65\lambda_0$, the point where the toe typically starts to move down the wave face. Just after $X_{wm} = 5.65\lambda_0$, u_{max} typically becomes greater than U_{crest} and increases rapidly thereafter. The highest measured values of u_{max} are about $1.4U_{crest}$. Since each data point comes from a separate experimental run, the range in the data at each X_{wm}/λ_0 is a reflection of the randomness in the flow-field development. As can be seen from the figure, this range increases rapidly just after $X_{wm} = 5.65\lambda_0$. This increased range and the presence of vorticity at this stage of the breaking process is indicative of the onset of turbulent flow.

In figure 16, the dimensionless total circulation in the crest region ($\Gamma/U_0\ell_c$) is plotted against the scaled distance from the wavemaker, where $U_0 = g/(2\pi f_0)$ is the average wave phase speed calculated by linear wave theory and $\ell_c = \sqrt{T/g}$ is the

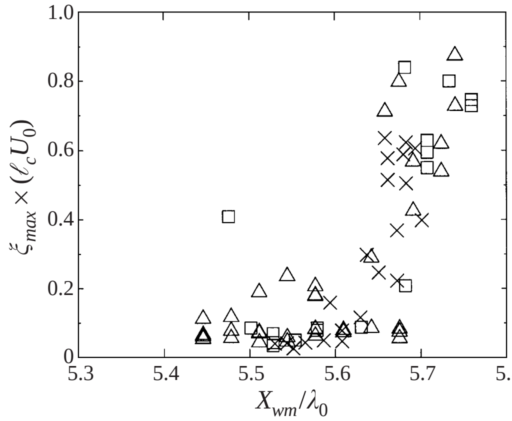

FIGURE 17. Comparison of scaled maximum vorticity, $\zeta_{max}\ell_c/U_0$, versus X_{wm}/λ_0 for three wave frequencies. ×, $f_0 = 1.15$ Hz; □, $f_0 = 1.26$ Hz; △, $f_0 = 1.42$ Hz.

Flow fields	Percentage average difference (X and Y components)	Percentage r.m.s. of difference
Figures 5(*e*) and 18	(−3.76, −0.70)	2.32
Figures 5(*f*) and 18	(−4.30, −1.20)	2.16

TABLE 4. Average and root-mean-squared differences of velocity vectors (in the reference frame moving with the crest) of the 1.15 Hz and 1.42 Hz waves when they are at about the same stage of breaking. The velocity differences have been scaled with the average of the crest phase speeds of the 1.15 Hz and 1.42 Hz waves and are expressed as percentages.

capillary length scale. This scaling of the circulation was chosen based on the surface profile results in Duncan *et al.* (1999) which showed that the lengths of the bulge and capillary waves before the toe motion began, scaled with ℓ_c. Thus, in choosing the above non-dimensionalization of Γ it has been assumed that the initial size of the turbulent patch scales with the lengths of the surface undulations before the turbulent flow is generated and that the velocity scale is proportional to the wave phase speed. In figure 16, the data for the 1.15 Hz wave with $A/\lambda_0 = 0.0502$ have been shifted by $0.1\lambda_0$ in the same manner as in figure 15. The data for all three wave frequencies show the same trend. The circulation stays very low until a sudden increase in positive (counterclockwise) circulation occurs at about $X_{wm}/\lambda_0 \approx 5.65$. This is the same X_{wm}/λ_0 where the maximum horizontal particle velocity increased above U_{crest}. The sudden generation of circulation is qualitatively the same for all the waves. It would be interesting to know how the maximum total circulation generated by the breakers varies with f_0. These total circulation values would appear in figure 16 as new levels of constant Γ that would probably be reached for high enough X_{wm}/λ_0. Unfortunately, as can be seen from the figure, the circulation has not clearly levelled off at the largest values of X_{wm}/λ_0 in the present measurements.

The scaled maximum vorticity, $\zeta_{max}\ell_c/U_0$, in each flow field is plotted versus X_{wm}/λ_0 in figure 17. As in figures 15 and 16, the data for the 1.15 Hz wave with $A/\lambda_0 = 0.0502$ have been shifted horizontally by $0.1\lambda_0$. With the exception of a few data points, the maximum vorticity is small for $X_{wm}/\lambda_0 < 5.65$ and increases rapidly thereafter. The data for the three frequencies look very similar.

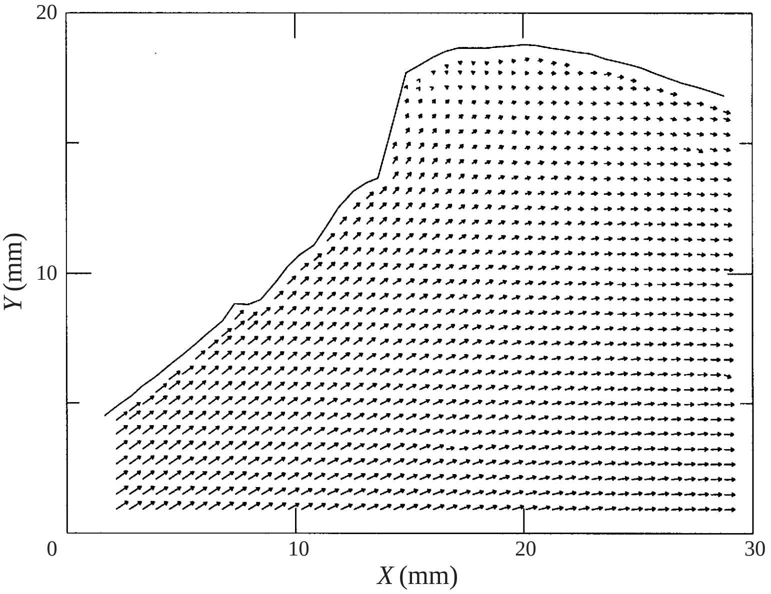

FIGURE 18. The velocity field for the $f_0 = 1.15\,\text{Hz}$ $A/\lambda_0 = 0.0497$ wave at $X_{wm}/\lambda_0 = 5.51$.

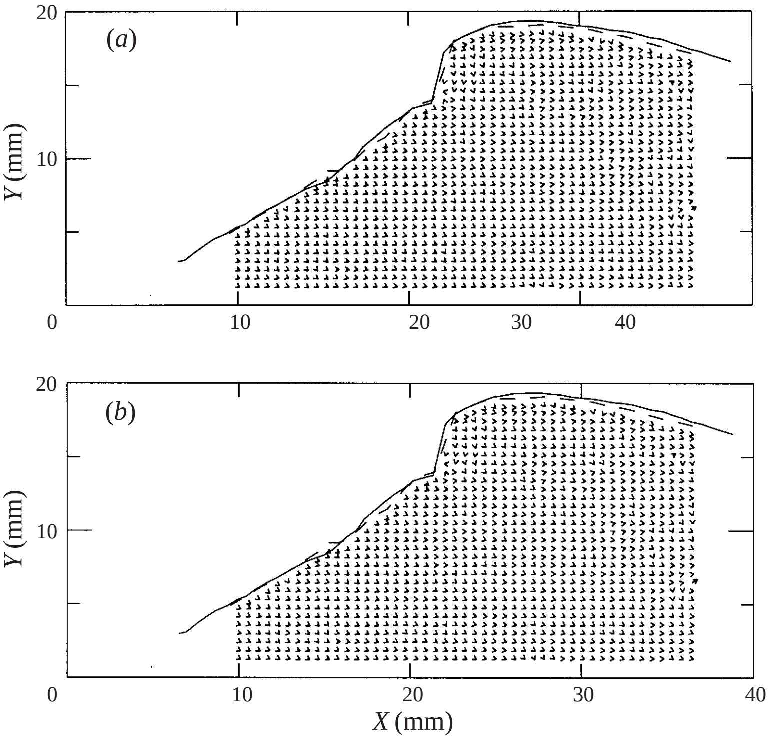

FIGURE 19. (*a*) The difference of velocity vectors relative to the crest between those in figures 18 and 5(*e*). Solid and dashed lines are the surface profiles in figures 5(*e*) and 18 respectively. The average and r.m.s. of the percentage difference are given in table 4. (*b*) As (*a*) but the difference between figures 18 and 5(*f*).

It was shown in Duncan *et al.* (1999) that for times before the toe begins to move, the shape of the free surface at the crest is independent of wave frequency. In the following, a similar comparison is made for the flow fields. In particular, a flow field of one of the 1.15 Hz waves (see figure 18) is compared to the two flow fields of the 1.42 Hz wave depicted in figures 5(*e*) and 5(*f*). By examining the surface profiles in these figures it can be seen that the waves are in about the same breaking stage. To compare the flow fields, the velocity vector field from the 1.15 Hz wave is subtracted from the velocity fields of the 1.42 Hz wave. Before performing the subtraction, the flow fields (taken in the reference frame moving with the wave crests) were aligned by comparison of the surface profiles. The differences of the flow vectors were then scaled with the average of the crest speeds of the 1.15 Hz and 1.42 Hz waves, $\overline{V}_c$. The resulting difference flows are given in figures 19(*a*) and 19(*b*) and the average and root-mean-squared velocity differences are given (as percentages) in table 4. As can be seen from the table, the average of the difference of the velocity vectors is about 4%, and the r.m.s. of these differences are about 2.2%. These differences should be compared to the average fluid speed in the region of the crest of all three waves, $0.34\overline{V}_c$, and the difference in the crest phase speeds for the two wave frequencies, $0.18\overline{V}_c$. Considering that the flow vectors obtained in the present PIV measurement have an uncertainty of 1–3% and that the two flow fields compared might not be in exactly the same breaking stage, it is estimated that the experimental error in this comparison could be around 6%. Thus, the data above show that the flow fields in the 1.15 Hz and 1.42 Hz waves are quantitatively the same within the range of experimental error.

For times after the toe motion has begun, the flow fields and vorticity patterns are also quite similar for all three wave frequencies. As examples, vorticity contours for the 1.15 Hz and 1.26 Hz waves at large X_{wm}/λ_0 are given in figures 20(*a*) and figures 20(*b*), respectively, for comparison with similar contours for the 1.42 Hz wave in figures 12(*b*), 14(*b*) and 14(*d*). As can be seen from the figures, the positions, lengths and thicknesses of the vortical layers are qualitatively the same for all three waves.

5. Conclusions

Flow fields in the crests of gentle spilling breakers were studied experimentally with particle image velocimetry (PIV). The spatial resolution of the measurements was 0.58 mm. Froude-scaled generation conditions were used to produce waves with three characteristic frequencies: $f_0 = 1.42$, 1.26, and 1.15 Hz. The waves were identical to those for which the crest profile evolution was studied by Duncan *et al.* (1999). In the former study, it was found that the breaking process is initiated by the formation of a bulge on the forward face of the wave. The leading edge (toe) of the bulge initially remains in a steady position relative to the crest. The present measurements show no vorticity and no evidence of a recirculating region under the bulge during this initial phase of the breaking process. Instead, the flow patterns resemble those under a finite-amplitude wave system. The instantaneous flow fields near the crests of waves with different f_0 were found to be quantitatively the same in the reference frame moving with the crest to within the range of experimental error. A short time after the bulge first appears, a new phase of the breaking process is initiated when the toe begins to move down the wave face. The maximum horizontal component of the fluid velocity approaches the wave phase speed at about the time that the toe begins to move. The location of this maximum velocity component is near the

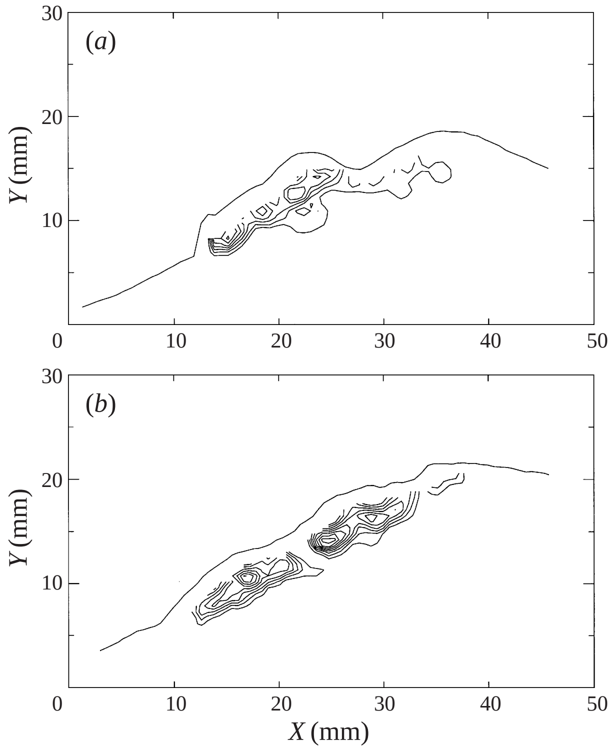

FIGURE 20. An instantaneous vorticity field for (*a*) the $f_0 = 1.15\,\mathrm{Hz}$, $A/\lambda_0 = 0.0497$ wave, $X_{wm}/\lambda_0 = 5.68$; and (*b*) the $f_0 = 1.26\,\mathrm{Hz}$ wave, $X_{wm}/\lambda_0 = 5.73$. Minimum and incremental levels of vorticity are $\omega_{\min} = 40\,\mathrm{s}^{-1}$ and $\Delta\omega = 40\,\mathrm{s}^{-1}$.

surface about halfway between the toe and the crest. After the toe begins to move, the fluid velocities found near the free surface in the zone between the toe and the crest increase rapidly; horizontal components as high as 1.4 times the crest speed were found. Vorticity first appears a little downstream of the toe just after the toe begins to move and, as the breaking process continues, the vortical region extends progressively from the toe to the crest. During this time, the crest moves about twice the total length of the vortical region. The total circulation increases rapidly while the toe is moving and reaches values as high as $4.6U_0\ell_c$ where $U_0 = g/(2\pi f_0)$ and $\ell_c = \sqrt{T/g}$, where T is the surface tension divided by the density of water. However, it should be kept in mind that the circulation may still be increasing at the time of the last measurements reported herein.

The support of the Office of Naval Research under contracts N0001490J1977 (Program monitor: Dr E. Rood) and N000149610474 (Program monitor: Dr D. Trizna) is gratefully acknowledged. The authors would also like to express their gratitude to NSWC, Carderock for supplying the Nd:YAG lasers and to S. Eisen, H. Yoshida and D. Coakley who helped in taking the PIV pictures.

Appendix A

In this Appendix, the theory of Longuet-Higgins (1992) is used to compute the thickness (δ_c), mean vorticity ($\overline{\omega}_\infty$), and induced velocity ($\overline{u}_0$) of the boundary layer

Phase	λ_0(cm)	a(cm)	t(s)	ak	σ (s^{-1})	δ (cm)	$\overline{\varpi}_\infty$ (s^{-1})	$\overline{u}_0$ (cm s^{-1})
Phase 1	0.38	0.030	0.06	0.50	574.7	0.0064	181.6	7.6
Phase 2	0.28	0.060	0.08	1.35	908.2	0.0052	2092.2	64.2

TABLE 5. Vorticity generation and boundary-layer thickness at the first wave in the capillary wavetrain. Phase 1 is before the toe motion begins and Phase 2 is during the beginning of the toe motion.

under the capillary waves found upstream of the toe. In § 7 of Longuet-Higgins (1992), the lengthscale associated with the vorticity generation at the free surface of the capillary waves is

$$\delta = (2\nu/\sigma)^{1/2}, \tag{A 1}$$

where ν is the kinematic viscosity of water and σ is the radian frequency of the capillary wave. The mean vorticity shed into the stream (Longuet-Higgins 1992 equation (7.6)) is

$$\overline{\varpi}_\infty = -1.264(ak)_0^2\sigma, \tag{A 2}$$

where $(ak)_0$ is the slope of the first wave ahead of the toe (a is the wave amplitude measured from the trough to the crest and $k = 2\pi/\lambda$ where λ is the wavelength). The additional flow speed induced at the mean water level by the viscous boundary layer is (Longuet-Higgins 1992 equation (7.7))

$$\overline{u}_0 = 0.87(ak)_0^2 c, \tag{A 3}$$

where c is the phase speed of the capillary waves.

Measurements of the capillary waves for the 1.42 Hz wave given in figure 18 of Duncan *et al.* (1999) will be used in the following calculations. The calculations are performed for two phases of the process: before the toe begins to move, and just after the toe begins to move. The time between the capillary waves first being visible and the toe first beginning to move is about 0.06 s (see figure 18(*a*) of Duncan *et al.* 1999). During this time, the amplitude of the capillary wavetrain increases with time and decays sharply from the toe in the upstream direction. The time average of the amplitude of the first capillary wave is about 0.03 cm while the average of the length of this wave is about 0.38 cm. Estimates of δ, $\overline{\varpi}_\infty$ and $\overline{u}_0$ obtained with the above data and equations (1) to (3) are given in table 5. In these estimates, we have used $\nu = 0.012\,\mathrm{cm}^2\,\mathrm{s}^{-1}$, $\sigma = \sqrt{Tk^3}$ (where $T = 73\,\mathrm{cm}^3\,\mathrm{s}^{-2}$ is the surface tension coefficient), and $c = \sigma/k$. The thickness of the layer over which the vorticity diffuses can be estimated from figure 9 of Longuet-Higgins (1992). To obtain this estimate, it is necessary to compute the number of cycles $N = \sigma t/(2\pi)$ during the lifetime of the capillary waves. Using the above data, it is found that $N \approx 5$ and according to figure 9 of Longuet-Higgins (1992) this corresponds to a boundary-layer thickness of about 8δ or 0.051 cm.

The second line of table 5 gives the capillary-wave and theoretical boundary-layer data for the period just after the toe begins to move down the wave face. The capillary data, taken from Duncan *et al.* (1999), covers the period between the time that the toe motion begins and the time when, owing to three dimensionality of the flow, the capillary wave measurements are no longer feasible (a duration of about 0.015 s). As can be seen from the table, $\overline{\varpi}_\infty$ and $\overline{u}_0$ are quite large. On the other hand, the number of capillary wave cycles during this phase of the capillary development is only $N = 0.015\sigma/(2\pi) = 2.2$. From figure 9 of Longuet-Higgins (1992), this corresponds to a layer thickness of only $2\delta = 0.104$ mm. When added to the previously calculated boundary-layer thickness for the capillary development before the toe motion began, we obtain about 0.6 mm.

REFERENCES

Adrian, R. J. 1991 Particle-imaging techniques for experimental fluid mechanics. *Ann. Rev. Fluid Mech.* **23**, 261–304.

Cowen, E. A. & Monismith, S. G. 1997 A hybrid digital particle tracking velocimetry technique. *Exps. Fluids* **22**, 199–211.

Dabiri, D. & Gharib, M. 1997 Experimental investigation of the vorticity generation within a spilling water wave. *J. Fluid Mech.* **330**, 113–139.

Duncan, J. H., Philomin, V., Qiao, H. & Kimmel, J. 1994*b* The formation of a spilling breaker. *Phys. Fluids* **6**, S2.

Duncan, J. H., Qiao, H., Behres, M. & Kimmel, J. 1994*a* The formation of a spilling breaker. *Phys. Fluids* **6**, 2558–2560.

Duncan, J. H., Qiao, H., Philomin, V. & Wenz, A. 1999 Gentle spilling breakers: crest profile evolution. *J. Fluid Mech.* **379**, 191–222.

Gharib, M. & Weigand, A. 1996 Experimental studies of vortex disconnection and connection at a free surface. *J. Fluid Mech.* **321**, 59–86.

Hjelmfelt, A. T. & Mockros, L. F. 1966 Motion of discrete particles in a turbulent fluid. *Appl. Sci. Res.* **16**, 149–161.

Keane, R. D. & Adrian, R. J. 1992 Theory of cross-correlation analysis of PIV images. *Appl. Sci. Res.* **49**, 191–215.

Lin, J. C. & Rockwell D. 1995 Evolution of a quasi-steady breaking wave. *J. Fluid Mech.* **302**, 29–44.

Longuet-Higgins, M. S. 1992 Capillary rollers and bores. *J. Fluid Mech.* **240**, 659–679.

Longuet-Higgins, M. S. 1996 Capillary jumps on deep water. *J. Phys. Oceanogr.* **96**, 1957–1965.

Longuet-Higgins, M. S. & Cleaver, R. P. 1994 Crest instabilities of gravity waves. Part 1. The almost-highest wave. *J. Fluid Mech.* **258**, 115–129.

Rood, E. P. 1994 Interpreting vortex interactions with a free surface. *Trans. ASME* I: *J. Fluids Engng* **116**, 91–94.

Rood, E. P. 1995 Free surface vorticity. In *Free-Surface Vorticity* (ed. S. Green), chap. 17. Kluwer.

Stokes G. G. 1847 On the theory of oscillatory waves. *Mathematics and Physics*, *Papers 1*. Cambridge University Press, 1880.